CHEMISTRY

One-step separation of lithium from natural ores in seconds

Shichen Xu[1]†, Justin Sharp[1]†, Alex Lathem[1,2], Qiming Liu[1], Lucas Eddy[1,2], Weiqiang Chen[3,4,5], Karla J. Silva[1], Shihui Chen[1], Bowen Li[1], Tengda Si[1], Jaeho Shin[1], Chi Hun Choi[6], Yimo Han[6], Kai Gong[3,4,5], Boris I. Yakobson[1,2,6,7], Yufeng Zhao[6,8]*, James M. Tour[1,2,5,6,7]*

Lithium (Li), the lowest-density metal, is an optimal element in most battery designs. With the increasing demand for Li, metallurgical techniques using excess acid leaching of mineral ores are common. However, these techniques are limited by multistep processes with adverse environmental impacts caused by secondary waste streams. Here, we show a one-step, acid-free, and alkali-free extraction process for Li from mineral ores with an initial Li content of only 4.8%. By applying flash Joule heating to α-spodumene under an atmosphere of Cl_2 (FJH-Cl_2), LiCl immediately distills from the remaining nonvolatile aluminum and silicon oxides. LiCl with a 97% purity and 94% yield can be achieved, enormously reducing costs and waste emissions. Local processing with FJH-Cl_2 can markedly lessen the complexity and cost of obtaining Li, obviating remote mining and facilitating the world's progression toward cleaner renewable energies, which also paves the way for extracting critical metals from other mineral ores.

INTRODUCTION

Li is an essential component in lithium-ion and lithium-metal batteries, which account for most portable renewable energy storage systems, facilitating the ubiquitous internet of things and electric vehicles (*1*, *2*). This has led to a global surge in Li demand (*3*). The supply of Li, however, is confronted with obstacles, including a lack of raw materials, the need for remote mining, environmental concerns, and the complexity of Li extraction and separation (*1*, *4*). Efficient separation of Li is crucial to prevent supply chain disruptions and to minimize secondary waste streams while economically incentivizing the mining industry (*5*, *6*). Primary natural sources of Li are in brine deposits and mineral ores (fig. S1, A and B) (*7*–*12*). Two-thirds of Li that is processed worldwide is extracted from brines although the separation process is slow, taking 12 to 18 months in large-area evaporation ponds, and brines have low Li concentrations of only 1 to 2 wt % (*9*, *13*). Conversely, Li ores such as spodumene, lithium aluminum inosilicate, $LiAl(SiO_3)_2$, have double the Li content of brines, reaching ~4 wt % of the complex and ~8 wt % of the total metal content in the ore. However, only one-third of Li that is obtained worldwide is extracted from spodumene because of the increased complexity in isolation using this ore instead of brines (*8*, *14*–*16*). Many wet strategies, including H_2SO_4 roasting (*17*–*21*), fluorination (*22*, *23*), chlorination (*24*, *25*), carbonation (*14*, *26*, *27*), froth flotation (*28*–*30*), and electrochemical leaching (*31*), have been used to separate Li from spodumene. Among them, the H_2SO_4 roasting process has been the standard method for Li separation from mineral ores including spodumene, but H_2SO_4 roasting requires extended heating cycles up to 1100°C, excess acid, and several chemical additives while generating cumbersome secondary waste streams as seen in fig. S1A (*17*–*25*).

Flash Joule heating (FJH) is an ultrafast, controllable, and energy-efficient method that has been used for materials synthesis (*32*–*34*), waste upcycling (*35*–*37*), and recovery of metals (*38*, *39*). We show here that FJH allows spodumene to be converted from α-phase to β-phase in seconds, and LiCl separation can ensue using only 1 M HCl (Method A). However, this method still requires the use of diluted acid. Conversely, we can combine FJH with a gas chlorination process (FJH-Cl_2) as an alternative method of Li separation (Method B) (Fig. 1A). When chlorine gas (Cl_2) enters the chamber and is flash Joule heated in <1 s, Li from the spodumene reacts with the Cl_2 to form volatile LiCl that distills from the unreacted silicon and aluminum oxides (Fig. 1B). FJH-Cl_2 reduces the ore processing time to seconds instead of the days needed for H_2SO_4 roasting and the 12 to 18 months needed when processing Li brines by evaporation (fig. S1B).

RESULTS

Arc welder FJH apparatus

A commercial arc welder with a maximum power output of 5.8 kW can power the laboratory-scale system (fig. S2), providing a rapid and stable electrical heat source for the reaction. The first advantage of this setup is temperature controllability, achieved by adjusting the current setting on the arc welder dial (Fig. 1C). When the temperature profile of the unloaded carbon paper platform is measured using an infrared thermometer, the temperature is ~1150°C at a current output setting of 10 and ~1630°C at a current setting of 20. The sample is heated through thermal conduction from the carbon paper, and thus its temperature is slightly lower than that of the carbon paper itself. When the current setting is 15, the top surface temperature of the carbon paper reaches 1420°C, whereas the surface temperature of the loaded sample is ~1340°C (fig. S3). Second, there is temperature uniformity. The surface of the heated carbon paper displays a uniform orange-red color, confirming a constant temperature induced by FJH across the carbon paper as verified with an infrared thermometer (Fig. 1D and fig. S4). Although minor temperature

[1]Department of Chemistry, Rice University, Houston TX 77005, USA. [2]Applied Physics Program and Smalley-Curl Institute, Rice University, Houston, TX 77005, USA. [3]Department of Civil and Environmental Engineering, Rice University, 6100 Main Street, Houston, TX 77005, USA. [4]The Ken Kennedy Institute, Rice University, 6100 Main Street, Houston, TX 77005, USA. [5]Rice Advanced Materials Institute, Rice University, 6100 Main Street, Houston, TX 77005, USA. [6]Department of Materials Science and NanoEngineering, Rice University, Houston, TX 77005, USA. [7]NanoCarbon Center and the Rice Advanced Materials Institute, Rice University, Houston, TX 77005, USA. [8]Department of Physics, Corban University, 5000 Deer Park Drive SE, Salem, OR 97317, USA.
*Corresponding author. Email: tour@rice.edu (J.M.T.); yzhao@corban.edu (Y.Z.)
†These authors contributed equally to this work.

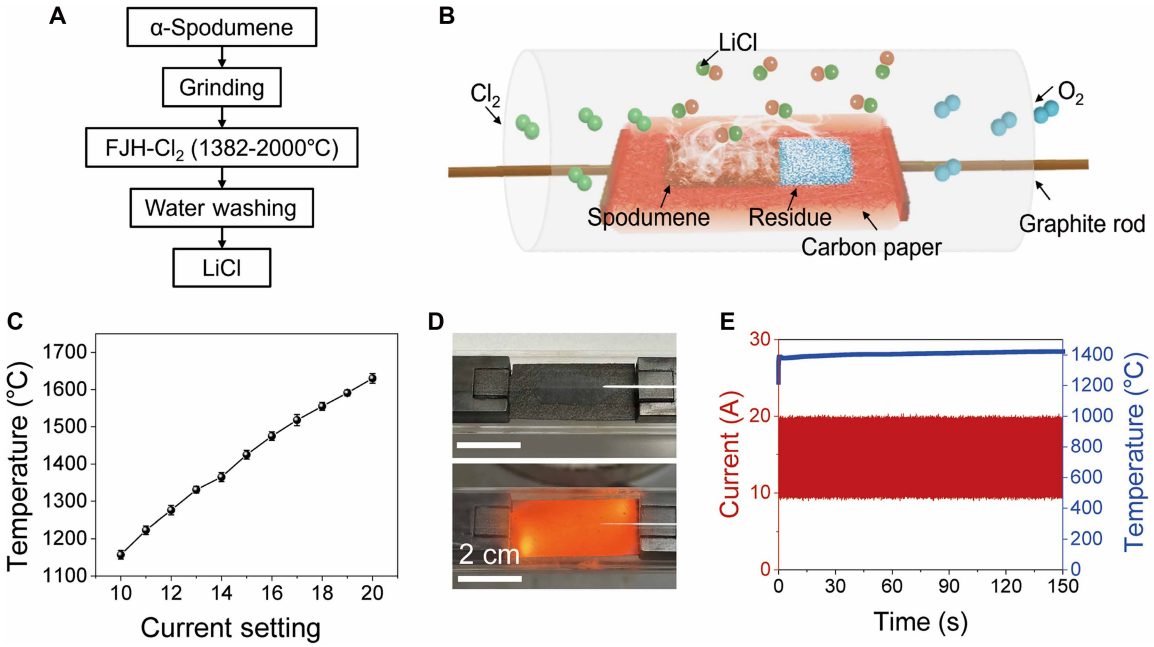

Fig. 1. FJH-Cl_2 for separation and recovery of Li. (**A**) Process flow of the Li separation from spodumene by the FJH-Cl_2 method. (**B**) Schematic diagram of the FJH-Cl_2 process, where spodumene is placed on the carbon paper and reacts with Cl_2. Generated LiCl evaporates and condenses on the inner surface of the quartz tube, whereas the unreacted silicon and aluminum oxide residues remain on the carbon paper. (**C**) Temperature plot with increasing current settings from 10 to 20. This current setting is in arbitrary units on the dial and is approximately but linearly modulating the current setting in the arc welder. All error bars represent the SD, where $N = 5$. (**D**) Pictures of carbon paper before (top) and during (bottom) FJH. (**E**) Real-time temperature (blue) and current (red) with a current setting of 15 for 150 s. Notice the temperature rise to >1380°C in <1 s.

variations may arise due to inconsistencies in the carbon paper quality, the overall surface temperature deviation remains within 2 to 3%. Third, there is temperature stability. When the current setting is 15, the voltage remains stable at 14 V (fig. S5), whereas the current output is 15 ± 5 A due to the high-frequency switching of the arc welder. The resistance of carbon paper is maintained at ~1 ohm, maintaining a stable temperature at each current setting. The surface temperature of the carbon paper remains at 1420°C for 150 s, which allows us to realize the separation by only one step (Fig. 1E and table S1). Benefiting from resistive heating, the carbon paper system exhibits rapid heating and cooling rates when powered by an arc welder (fig. S6). After the current is cut off at the end of the reaction, the temperature drops below 1000°C within a few hundred milliseconds, which is insufficient to sustain the chlorination reaction (fig. S7).

Conversion of α-spodumene to β-spodumene

Spodumene exists in different crystalline phases, typically in its natural α-phase or rock form (Fig. 2A). Before the FJH process, the spodumene rock was ground into micrometer-sized powder using a mortar and pestle and then sieved through successive meshes with pore sizes of 1000, 200, and 53 μm to obtain particles of corresponding sizes, which were classified here as large, medium, and small particles. Scanning electron microscopy (SEM) images show these particles as uniformly sized but irregularly shaped (Fig. 2A and fig. S8). The particle size distribution of the three sieved spodumene samples is measured by combining laser diffraction/scattering and dynamic image analysis (Fig. 2A, text S1, and fig. S8). The particles sieved through a 53-μm mesh have an average size of 28.59 μm, with D50 and D90 values of 22.42 and 62.36 μm, respectively (Fig. 2B). When spodumene particles are subjected to FJH, the α-phase converts to the β-phase. The x-ray diffraction (XRD) pattern shows that the two phases are clearly different (Fig. 2C) (*40*). However, the complete phase transformation varies with different particle sizes due to inefficient heat transfer with large particles (figs. S9 and S10). When small-sized particles (average size at 28.59 μm) are subjected to 30 s of FJH at 1150°C, only the β-phase signal is observed after the treatment (Fig. 2C). The Raman spectroscopy further illustrates that the untreated α-phase exhibits typical Raman peaks ~370 and 700 cm^{-1}. The small particles treated by FJH only show the characteristic Raman peak of the β-phase at ~500 cm^{-1} (Fig. 2D) (*41*, *42*). However, using FJH and 1 M HCl treatment (Method A; figs. S11 and S12) has a greater effect on improving the LiCl yield than the purity. When the spodumene average size is 28.59 μm, the yield of Li increased from 56.6% before FJH to 90.2% after FJH with 1 M HCl extraction (fig. S12).

FJH-Cl_2 of spodumene

FJH can afford the formation of β-spodumene in seconds, which is necessary to increase the efficiency of Li extraction. However, this cannot eliminate the use of acid nor does it overcome the limitations in the purity of Li. Therefore, exploring the chemical reactivity of different elements in spodumene is necessary to achieve efficient Li separation. Inductively coupled plasma mass spectrometry (ICP-MS) results show that the main elements in the spodumene rock are Li, Al, and Si, with Li accounting for 4.8% of the total content of these three elements (Fig. 3A and text S2). This is consistent with SEM with energy-dispersive x-ray spectroscopy (SEM-EDX) (fig. S13) and

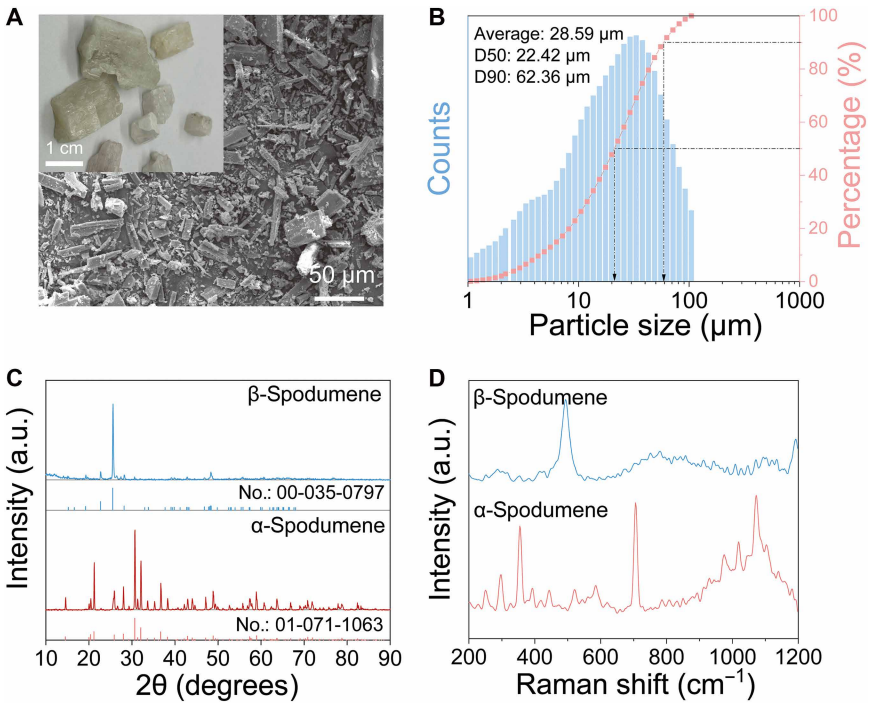

Fig. 2. Phase transformation of spodumene. (**A**) SEM image of ground spodumene powder sieved by a 53-μm mesh with an average particle size of 28.59 μm. The inset image is the raw α-spodumene sample as received. (**B**) Size distribution of sieved and ground spodumene particles. The average size is 28.59 μm, and the D50 and D90 are 22.42 and 62.36 μm, respectively. This means that 50% of the sample has a size of 22.42 μm or smaller, and 90% of the sample has a particle size of 62.36 μm or smaller. (**C**) XRD pattern and (**D**) Raman spectra of the spodumene before and after phase transformation, where the α-phase (red) is present before heating and the β-phase (blue) is present after FJH at 1150°C. a.u., arbitrary units.

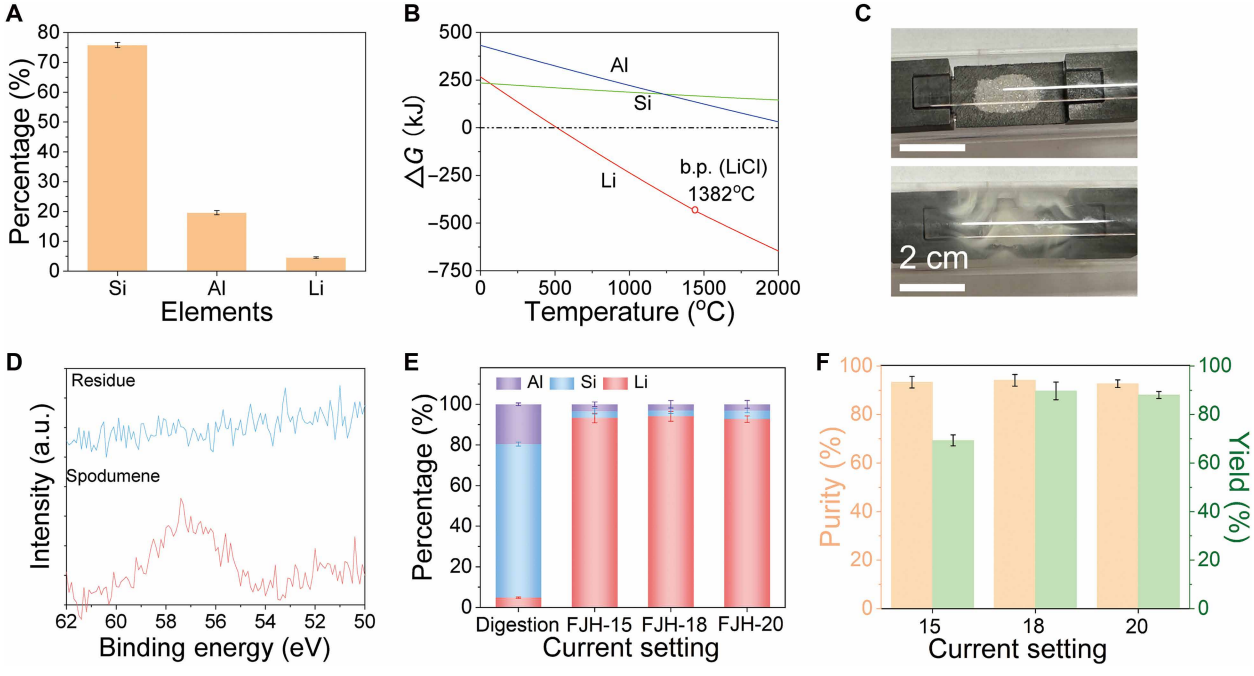

Fig. 3. Separation and recovery of Li from the spodumene by FJH-Cl_2. (**A**) The ICP-MS results of the raw spodumene show the Li concentration related to Si and Al. (**B**) Thermodynamic analysis of the chlorination reaction of metal oxides. Only the chlorination of Li_2O is feasible above 514°C when the ΔG is negative (below the black dotted line). b.p., boiling point. (**C**) Picture of the quartz tube containing spodumene before (top) and after (bottom) FJH-Cl_2 when LiCl (white volatile) has condensed inside the quartz tube. (**D**) XPS spectra of spodumene before (red) and residue after (blue) FJH-Cl_2. The Li 1s signal is only detected before FJH-Cl_2. (**E**) The composition of Li, Si, and Al in raw spodumene and the volatile phase after FJH-Cl_2 are shown for each of the three current settings. (**F**) Purity (orange) and yield (green) of LiCl after FJH-Cl_2 of spodumene at current settings of 15, 18, and 20 for 30 s each. All error bars in (A), (E), and (F) represent the SD, where $N = 3$.

x-ray photoelectron spectroscopy (XPS) (fig. S14) results. We conducted a thermodynamic analysis for chlorinating silicon oxide (SiO_2), aluminum oxide (Al_2O_3), and lithium oxide (Li_2O). According to the Gibbs free energy change (ΔG) versus temperature, only Li_2O is chlorinated below 2000°C, whereas chlorination does not occur for SiO_2 and Al_2O_3 within that temperature range (Fig. 3B and table S2). ΔG is negative for Li_2O when the temperature exceeds 514°C, suggesting that Li in spodumene can be chlorinated at ~514°C. However, when the chlorination reaction occurs between 514°C and the boiling point of LiCl (1382°C), leaching the formed LiCl with water results in low purity and yield of Li due to the interference of Si and Al impurities in the sample (fig. S15). However, when the control temperature is above the boiling point of LiCl and below 2000°C, LiCl can be cleanly volatilized and separated from spodumene (Fig. 1C).

When the arc welder settings are 15, 18, and 20, the corresponding temperatures are 1420°, 1550°, and 1630°C, respectively. After 30 s of chlorinating spodumene, volatile LiCl deposits on the inner surface of the quartz tube (Fig. 3C). SEM-EDX characterization results indicate that the primary element in the volatile fraction is Cl, with trace amounts of Si and Al (fig. S16A); Li is too light to be detected. XPS results also show that the main elements in the volatile fraction are Cl, O, and Li (fig. S16, B and C). After the chlorination reaction, a substantial amount of residue remains on the carbon paper. SEM-EDX, XPS, and XRD results reveal that the main elements in the residue are Si, Al, O, and Cl (figs. S17 and S18). By comparing the XPS fine spectra of Li in the original spodumene sample with the residue, there is no detectable Li signal in the residue after FJH-Cl_2 (Fig. 3D). This result suggests that the FJH-Cl_2 reaction can selectively and efficiently separate Li as LiCl directly from raw spodumene. The residue can be easily removed without surface degradation (fig. S19).

High-temperature vapor-phase reactions can inevitably introduce SiO_2 and Al_2O_3 into the volatile phase via physical mass transport processes during the rapid LiCl volatilization; in an industrialized process, further fractionation plates would be desired. ICP-MS results show that purity can be enhanced when the volatile obtained from the chlorination reaction is rinsed with water (Fig. 3E). LiCl is water soluble whereas SiO_2 and Al_2O_3 are not (table S2), so the water wash acts as an additional purification step while extracting only the condensed LiCl from the quartz tube. As a result, the purity of Li obtained from FJH-Cl_2 can reach 97% with an average purity of 94% (Fig. 3E). Furthermore, the yield of LiCl is related to the particle size of the sample and the chlorination temperature. As the particle size of the spodumene decreases, the yield of Li increases. When the particle size of spodumene is ~459 μm and the current dial is set to 18 (1550°C), the yield of Li obtained from 30-s FJH-Cl_2 is only 17% (fig. S20). With a particle size of ~143 μm, the yield of Li is slightly increased to 54% (fig. S21). However, when the particle size is reduced to ~28.3 μm, the yield of Li reaches 90%. The short reaction time allows smaller particles to provide a larger contact area with the gas, thereby markedly enhancing the efficiency and rate of metal extraction (Fig. 3F and fig. S20). Temperature influences both the thermodynamic driving force and the kinetic rate of reaction. When the particle size is ~28.3 μm and the arc welder setting is 15 (1420°C), the yield is still only 69.3% (Fig. 3F). However, when the current dial is set to 18 (1550°C), extracted LiCl with a maximum purity of 97% and an average purity of 94%, as well as a maximum yield of 94% and an average yield of 90%, can be obtained (Fig. 3F). Further increasing the temperature with a dial setting at 20 will introduce more Si and Al impurities into the volatile phase (Fig. 3F and figs. S22 to 25), leading to a slight decrease in purity. Moreover, higher temperatures inevitably lead to increased energy consumption (fig. S26 and table S3). Hence, when the temperature is set to 1550°C, the formation of LiCl occurs at ~514°C and its distillation at ~1382°C, which are favored both thermodynamically and kinetically. It is a common observation that one needs to exceed the boiling point of a material to increase its distillation rate, in this case 168°C, because the temperatures are so high relative to the surroundings.

Other sources of spodumene ore were used to ensure that the process worked equally well regardless of the region from which the sample was mined (*43*). Here, sand-like spodumene from Australia is used for Li extraction by FJH-Cl_2 (fig. S27 and text S3). When the Australian spodumene is ground to ~47-μm particle size and undergoes FJH-Cl_2, 90% purity and 89% yield of Li can be achieved at a current setting of 18 (figs. S28 to S31 and text S3). In addition, the team successfully achieved a scale-up from a 1-inch to a 3-inch system in the laboratory, allowing for gram-scale chlorination of spodumene. The separated Li reached a purity of 90% and a yield of 85% (figs. S32 and S33).

Density functional theory calculations

To understand why the chlorination method can so efficiently and quickly separate Li from spodumene, density functional theory (DFT) calculations were used to further explore the mechanism of this process. We compared three extraction pathways, including direct Li extraction from α-spodumene, direct Li extraction from β-spodumene, and transformation from α-spodumene to β-spodumene followed by Li extraction (Fig. 4 and figs. S34 to S36). The energy required to extract 100% of the Li between 1600 and 2000 K and at 1, 6, and 11 atm was calculated. Generally, natural spodumene is in the α-phase, which is monoclinic (Fig. 4A and fig. S35A); after extracting all the Li, the structure is different from the α-phase spodumene but still stable (Fig. 4B and fig. S35B). When increasing the temperature from 1600 to 2000 K and decreasing the pressure from 11 to 1 atm, the chlorination for extracting Li from α-phase spodumene requires less energy (Fig. 4C). During the FJH process, the spodumene readily converts from the monoclinic α-phase to the tetragonal β-phase (Fig. 4D and fig. S35C). After extracting the Li from β-phase spodumene, the structure frame (Fig. 4E and fig. S35D) is totally different from that of α-phase spodumene. Delithiation from the β-phase spodumene requires less energy than the α-phase under identical temperature and pressure (fig. S36). Because the phase transition from the α-phase to the β-phase is a thermodynamically favorable and exothermic process, the full delithiation energy is reduced by 0.30 eV/Li when considering the α-to-β phase transition followed by Li extraction from the β-phase (Fig. 4F and fig. S36), compared to direct delithiation from α-phase spodumene. This energy advantage accounts for the experimental observation that Li extraction occurs rapidly within just 30 s, although the starting material is α-phase spodumene. We propose that, during the FJH-Cl_2 process, spodumene undergoes a phase transition from α to β before reacting with Cl_2, thereby enabling a lower-energy pathway for Li separation.

LCA, TEA, and environmental impacts

A Monte Carlo life cycle assessment (LCA) and techno-economic analysis (TEA) were used, and the details are explained in text S4. The primary environmental and economic factors considered were energy consumption, greenhouse gas emissions of CO_2-eq listed as global warming potential (GWP), water consumption, and reagent

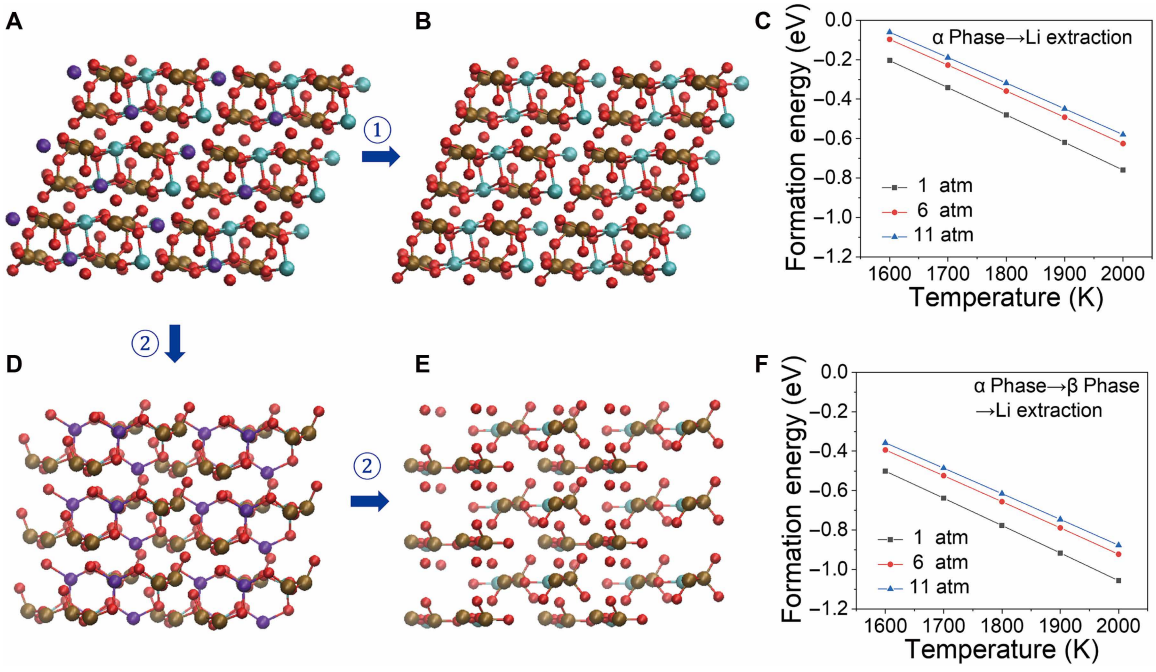

Fig. 4. DFT results for the delithiation energy of α-phase and β-phase spodumene. Side-view ball and stick model of α-phase spodumene before (**A**) and after (**B**) extracting 100% of Li. Red: O atoms; cyan: Al atoms; brown: Si atoms; violet: Li atoms. (**C**) Formation energy (Gibbs free energy) of delithiated α-phase spodumene at various temperatures and pressures. Side-view ball and stick model of β-phase spodumene before (**D**) and after (**E**) extracting 100% of Li. (**F**) Formation energy of phase transition from α-phase to β-phase spodumene followed by delithiation at various temperatures and pressures.

use, including acid, Cl_2, etc., and processing cost (Fig. 5 and tables S1 and S5 to S10). These factors were chosen because they contribute the most to the operating expenses (OpEx) materials costs, consumption, and produced waste. Compared to conventional H_2SO_4 roasting, a similar Li yield is achieved, and product purity is slightly lower than that achieved by traditional H_2SO_4 roasting and other methods, but the purity will likely increase as more theoretical plates are added upon scaling up. Processing 1 tonne of high-grade spodumene ore would produce 44 to 48 kg of Li for both methods because similar yields are achieved in both FJH-Cl_2 and H_2SO_4 roasting processes. The LCA shows that FJH-Cl_2 can reduce the process energy consumption by 77% from 15,900 to 3700 MJ (Fig. 5A). Water consumption is reduced by 67% from 373,000 to 125,000 kg if using the same relative amount needed for this laboratory process or 100% reduction of water if the equipment is industrialized at a longer evaporation distance, thereby inhibiting physical transport of the silicon or aluminum oxides with sufficient theoretical plates. Reagent consumption can be reduced by 93% and acid consumption can be 100% eliminated. However, these do not fully capture the improvement to the H_2SO_4 roasting method as intercontinental transportation of spodumene ore for processing substantially increases OpEx, which FJH-Cl_2 can eliminate. When accounting for intercontinental transportation in the H_2SO_4 roasting process, FJH-Cl_2 can reduce the GWP by up to 82% from 30,800 to 5600 kg CO_2 (Fig. 5B), and the TEA shows a reduction in OpEx of up to 81% from \$4900 to \$950 tonne^{-1} (Fig. 5, C and D).

DISCUSSION

Spodumene can be converted from the α-phase to the β-phase with only 30 s of FJH. An inexpensive arc welder can be used on a laboratory scale to facilitate this process. A FJH-Cl_2 method was demonstrated to separate Li with maximum purity of 97% and an average purity of 94%, as well as a maximum yield of 94% and an average yield of 90%. DFT calculations indicate that extracting Li from β-phase spodumene requires less energy, suggesting that spodumene converts first from the α-phase to the β-phase during the chlorination. LCA and TEA confirmed that the acid-free FJH-Cl_2 method can greatly reduce the total energy consumption, capital and operating costs, water consumption, and emissions compared to the industrial standard, H_2SO_4 roasting. Capitalizing upon the differences in ΔG_{form} of LiCl versus silicon and aluminum chlorides, these results showcase the FJH-Cl_2 method as an efficient and environmentally friendly process for Li separation from ores. Compared to the conventional capacitor-based Joule heating system, the continuous heating approach has huge potential for broader applications beyond e-waste recycling (table S4). This rapid Li separation method permits local Li assets to be developed, lessening transportation and processing costs for renewable energy transitions. Although the Li process here was only on a laboratory scale, FJH has recently been demonstrated on the production scale of 1 tonne day^{-1} for the conversion of inexpensive coal or coke into graphene at ~3000°C (*44*), a temperature nearly twice that needed for LiCl separation. Hence, with optimization of reactor designs, this process serves as a harbinger for clean and large-scale Li separation.

MATERIALS AND METHODS

Materials

The carbon paper was purchased from FuelCellStore (Toray Carbon Paper 060). Bulk spodumene crystals were purchased from EmpathMoonGems (Bulk Kunzite Spodumene Crystals), which are normally

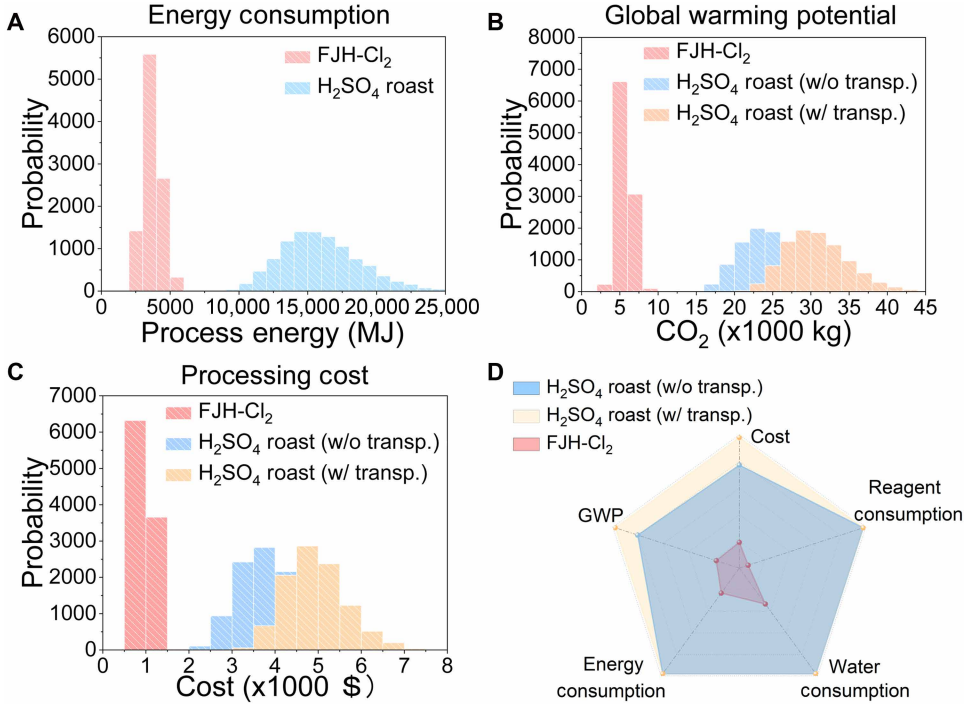

Fig. 5. LCA and TEA results for Li separation by H_2SO_4 roasting versus FJH-Cl_2 with (w/) or without (w/o) intercontinental transportation (transp.). Probability histograms for the (**A**) energy consumption in megajoules (MJ), (**B**) GWP in kilograms of carbon dioxide (kg CO_2), and (**C**) processing cost in US dollars necessary to produce 1 tonne of Li. The higher the probability and narrower the plotted histogram, the more accurate the prediction. (**D**) Radar plot simultaneously comparing the five key variables associated with the FJH-Cl_2 and industrial H_2SO_4 roasting processes to produce equal quantities of Li. For each Monte Carlo plot, N = 10,000 simulations.

sourced from one of the four locations: Afghanistan, Brazil, United States, or Madagascar (*45*). The spodumene sand was received from Australia. Both spodumene samples were ground into micrometer-sized powder using a mortar and pestle and then sieved through meshes with pore sizes of 1000, 200, and 53 μm to obtain particles of corresponding sizes. Nitric acid (HNO_3, 67 to 70 wt %, TraceMetal Grade, Fisher Chemical), hydrochloric acid (HCl, 37 wt %, 99.99%, trace metal basis, MilliporeSigma), hydrofluoric acid (HF, 48 wt %, 99.99%, trace metal grade for ICP analysis, MilliporeSigma), and ultrapure water (MilliporeSigma, ACS reagent for ultratrace analysis) were used for sample digestion. A Cl_2 cylinder (MilliporeSigma, 99.5%, 85 psi, 454 g) was used to supply the Cl_2. Argon gas (Airgas, 99.99%) was used to purge the system to remove moisture and air in the reaction chamber before the introduction of Cl_2. The arc welder power supply used as a DEKOPRO DKUS-MMA-160A arc welder (Amazon, $120) (*46*). The arc welder displays a "current" setting on the screen ranging from 8 to 160. Although the arc welder dial settings correspond to increasing current as they are turned higher, they are not an absolute current setting in amperes that matches with the dial setting number. The details of the FJH and FJH-Cl_2 system have been described previously (*47*).

Joule heating chlorination system

The Joule heating system comprises a power source, graphite rod, graphite block, and carbon paper. The power source is the commercial arc welder, connected to the carbon paper via graphite rods and graphite blocks. The temperature of the carbon paper was measured using a Micro-Epsilon thermometer, CTM-3SF75H2-C and CTRM-1H1SF100-C3. The former tests the temperature range between 200° and 1500°C, and the latter tests the temperature range between 1500° and 3000°C. The spodumene sample (50 mg) is spread evenly on the surface of carbon paper in a quartz tube and sealed at the ends of the tube with electrodes, an inlet chlorine gas line, and an outlet volatile gas line for unreacted chlorine. The quartz tube is conventionally 2.54 cm in interior diameter and 20 cm long. The size of carbon paper is usually 2 cm by 6 cm, and the resistance is 0.8 to 1.0 ohms. Argon gas (Airgas, 99.99%) is initially introduced into the chamber to purge the system atmosphere combined with a pumping system, and then chlorine gas (MilliporeSigma, 99.5%) is introduced into the reaction system. To eliminate the need to keep the Cl_2 cylinder valve open continuously, a reservoir is positioned between the Cl_2 cylinder and the gas pipeline, thereby reducing the risk of Cl_2 release in case of system failure. A CGA-180 fitting with a PTFE O-ring ensures a secure seal. Stainless steel is used for both tubing and fittings. To neutralize any unreacted Cl_2, the outlet is connected to two absorption traps: one containing solid sodium hydroxide (NaOH) and the other containing an aqueous NaOH solution. The gas chromatography–mass spectrometry (GC-MS) indicates that all the Cl_2 was absorbed by the trap, and the only detected gas was Ar (fig. S37). The entire system is in a well-ventilated hood. Note that, when industrialized, the unreacted Cl_2 can be easily recovered and reused (*48*, *49*).

Characterization

XRD was performed by the Rigaku SmartLab system with filtered Cu Kα radiation (λ = 1.5406 Å). Raman spectra were acquired using a Renishaw Raman microscope (laser wavelength of 532 nm, laser power of 5 mW, 50 × lens). SEM images were obtained using an FEI Quanta 400 ESEM FEG system at 20 kV. EDS spectra and maps were

acquired using the same system equipped with an EDS detector. XPS was conducted using a PHI Quantera XPS system at a base pressure of 5×10^{-9} torr. Elemental spectra were obtained with a step size of 0.1 eV with a pass energy of 26 eV. All the XPS spectra were calibrated using the standard C 1s peak at 284.8 eV. The particle size distribution of the spodumene powder was measured using a combined laser diffraction and dynamic image analysis system with Bettersizer S3 Plus instrument and software V8.20.

ICP-MS measurement

Total digestion is used to analyze the element content in raw spodumene. Fifty milligrams of raw samples was dissolved in a 5-ml solution of hydrochloric acid (HCl; 37 wt %, 99.99%, trace metal basis, MilliporeSigma), nitric acid (HNO_3; 67 to 70 wt %, TraceMetal Grade, Fisher Chemical), and hydrofluoric acid (HF; 48 wt %, 99.99%, trace metal grade for ICP analysis, MilliporeSigma) with a volume ratio of 3:1:1 and placed in an ultrasonic bath for 12 hours. The leaching experiment uses 30 mg of unreacted spodumene powder and 30 mg of FJH-treated powder in 5 ml of 1 M HCl for 6 hours at 90°C. For testing the volatile phase, the samples washed with deionized water are collected first, and then the supernatant is dissolved in 2 wt % dilute HNO_3, which is then diluted to target concentrations for ICP-MS testing. The Periodic Table mix 1 (MilliporeSigma, 33 elements of Al, As, Ba, Be, Bi, B, Ca, Cd, Cs, Cr, Co, Cu, Ga, In, Fe, Pb, Li, Mg, Mn, Ni, P, K, Rb, Se, Si, Ag, Na, Sr, S, Te, Tl, V, and Zn; 10 mg liter^{-1} each, in 10 wt % HNO_3 containing HF traces) and Periodic Table mix 2 (MilliporeSigma, 17 elements of Au, Ge, Hf, Ir, Mo, Nb, Pd, Pt, Re, Rh, Ru, Sb, Sn, Ta, Ti, W, and Zr; 10 mg liter^{-1} each, in 5% HF and 1% HCl containing HNO_3 traces) were used as the standard solution.

DFT computational methods

We perform DFT (*50*) modeling of FJH-Cl_2 delithiation of spodumene ($LiAlSi_2O_6$) as expressed in the following reaction

$$LiAlSi_2O_6 + (x/2)Cl_2 = xLiCl + Li_{(1-x)}AlSi_2O_6 \quad (1)$$

where $x = 0.5$ and 1.0, respectively, for 50 and 100% of Li atoms being extracted out of spodumene. The Gibbs free energy (formation energy) of the reaction can be calculated following the equation

$$G = \left[E_{\text{products}} - E_{\text{reactants}} + x\mu_{\text{LiCl}} - \left(\frac{x}{2}\right)\mu_{Cl_2}\right] / x \quad (2)$$

where E_{products} and $E_{\text{reactants}}$ are the DFT total energy of all products and reactants according to their chemical formula and stoichiometric ratio, and μ_{Cl_2} and μ_{LiCl} are the chemical potentials of Cl_2 and LiCl in gas phase. The chemical potential of Cl_2 gas as a function of pressure p and temperature T can be calculated following the equation (*51*)

$$\begin{aligned}\mu_{Cl_2}(T,p) = {} & H(T,p^0) - H(0\,\text{K},p^0) - \\ & T\left[S(T,p^0) - S(0\,\text{K},p^0)\right] + kT\ln\left(p/p^0\right)\end{aligned} \quad (3)$$

where the $p^0 = 1$ atm, and the entropy $S(T,p^0)$, enthalpy $H(T,p^0)$ are taken from the thermochemical tables (*52*). For LiCl, the same method is used.

DFT methods are used as they are implemented in the Vienna ab initio simulation package (VASP) (*53*). A plane-wave expansion up to 520 eV is used in combination with an all-electron–like projector augmented wave (PAW) potential (*54*). Exchange-correlation is treated within the generalized gradient approximation (GGA) using the functional parameterized by Perdew-Burke-Ernzerhof (*55*). Periodic condition is applied to the supercell or unit cell of crystal structures, with Brillouin zone integration converging over Monkhorst-Pack type mesh (*56*). In structure optimization using the conjugate-gradient algorithm as implemented in VASP, both the positions of atoms and the size of unit cells are fully relaxed so that the maximum force on each atom is smaller than 0.01 eV/Å.

The α-spodumene and β-spodumene crystal structures (*57*) were modeled in supercells each having 4 Li atoms, 4 Al atoms, 8 Si atoms, and 24 O atoms. We found that the overall frameworks of α-spodumene and β-spodumene remain to be stable except for slight deformation upon delithiation (see Fig. 4 and figs. S33 and S34, and the details of structural coordinates can be found in the data uploaded related to this paper). For the partially delithiated spodumene $Li_{(1-x)}AlSi_2O_6$ ($x = 0.5$), we searched the most energetically favorable structure in all possible configurations in which two of the four Li atoms in the original spodumene were removed. LiCl has an fcc (face-centered cubic) crystal structure with lattice constant of $a = 2.574$ Å, and the Cl_2 molecule is optimized inside a vacuum box of 20 Å by 20 Å by 20 Å.

LCA and TEA

The TEA and LCA were performed using Life Cycle Inventory (LCI) data from the European Reference Life Cycle Database (ELCD) with the CML-IA baseline impact assessment in the OpenLCA software (*58*). If not available in the ELCD database, LCI data were cited from the representative literature. As a preliminary estimate or "Class 4" estimate, Monte Carlo simulations were performed for both processes with 10,000 iterations at a 70% confidence interval (± 30% triangular distribution) for all variables according to the Association for the Advancement of Cost Estimating International (AACE International) (*59*). This nonamortized operating expense (OpEx) analysis was done to assess the necessary inputs to produce 1 tonne of Li from the FJH-Cl_2 and industrial H_2SO_4 roasting processes. The data used to simulate the spodumene H_2SO_4 roasting process were collected from the literature (*17*–*21*) to compare with experimental variables for the FJH-Cl_2 process. Data analysis from Monte Carlo simulations was performed with Microsoft Excel and Origin to plot the histograms and radar plots. The input and output materials for both processes are available in the attached Supplementary Materials; tables S5 to S10 are posted at Zenodo (see Data and materials availability).

Supplementary Materials

This PDF file includes:

Supplementary Text
Figs. S1 to S37
Tables S1 to S4
Legends for tables S5 to S10

REFERENCES AND NOTES

1. E. A. Olivetti, G. Ceder, G. G. Gaustad, X. Fu, Lithium-ion battery supply chain considerations: Analysis of potential bottlenecks in critical metals. *Joule* **1**, 229–243 (2017).
2. L. Trahey, F. R. Brushett, N. P. Balsara, G. Ceder, L. Cheng, Y. M. Chiang, N. T. Hahn, B. J. Ingram, S. D. Minteer, J. S. Moore, K. T. Mueller, L. F. Nazar, K. A. Persson, D. J. Siegel, K. Xu, K. R. Zavadil, V. Srinivasan, G. W. Crabtree, Energy storage emerging: A perspective from the Joint Center for Energy Storage Research. *Proc. Natl. Acad. Sci. U.S.A.* **117**, 12550–12557 (2020).
3. A. Alessia, B. Alessandro, V. G. Maria, V.-A. Carlos, B. Francesca, Challenges for sustainable lithium supply: A critical review. *J. Clean. Prod.* **300**, 126954 (2021).

4. C. Xu, Q. Dai, L. Gaines, M. Hu, A. Tukker, B. Steubing, Future material demand for automotive lithium-based batteries. *Commun. Mater.* **1**, 99 (2020).
5. B. K. Reck, T. E. Graedel, Challenges in metal recycling. *Science* **337**, 690–695 (2012).
6. T. E. Graedel, E. M. Harper, N. T. Nassar, P. Nuss, B. K. Reck, Criticality of metals and metalloids. *Proc. Natl. Acad. Sci. U.S.A.* **112**, 4257–4262 (2015).
7. S. Yang, F. Zhang, H. Ding, P. He, H. Zhou, Lithium metal extraction from seawater. *Joule* **2**, 1648–1651 (2018).
8. B. Tadesse, F. Makuei, B. Albijanic, L. Dyer, The beneficiation of lithium minerals from hard rock ores: A review. *Miner. Eng.* **131**, 170–184 (2019).
9. M. L. Vera, W. R. Torres, C. I. Galli, A. Chagnes, V. Flexer, Environmental impact of direct lithium extraction from brines. *Nat. Rev. Earth Environ.* **4**, 149–165 (2023).
10. Z. Li, C. Chen, L. Cao, X. W. Liu, K. W. Huang, Z. P. Lai, Lithium extraction from brine through a decoupled and membrane-free electrochemical cell design. *Science* **385**, 1438–1444 (2024).
11. M. Yong, M. Tang, L. Sun, F. Xiong, L. Xie, G. Zeng, X. Ren, K. Wang, Y. Cheng, Z. Li, E. Li, X. Zhang, H. Wang, Sustainable lithium extraction and magnesium hydroxide co-production from salt-lake brines. *Nat. Sustain.* **7**, 1662–1671 (2024).
12. G. Zhang, Y. Q. Li, X. Guan, G. L. Hu, H. Su, X. Xu, G. X. Feng, S. B. Shuchi, S. C. Kim, J. W. Zhou, R. Xu, X. Xiao, A. Wu, Y. Cui, Spontaneous lithium extraction and enrichment from brine with net energy output driven by counter-ion gradients. *Nat. Water* **2**, 1091–1101 (2024).
13. V. Flexer, C. F. Baspineiro, C. I. Galli, Lithium recovery from brines: A vital raw material for green energies with a potential environmental impact in its mining and processing. *Sci. Total Environ.* **639**, 1188–1204 (2018).
14. C. Dessemond, F. Lajoie-Leroux, G. Soucy, N. Laroche, J.-F. Magnan, Spodumene: The lithium market, resources and processes. *Minerals* **9**, 334 (2019).
15. A. Y. Fosu, N. Kanari, J. Vaughan, A. Chagnes, Literature review and thermodynamic modelling of roasting processes for lithium extraction from spodumene. *Metals* **10**, 1312 (2020).
16. H. Zhou, Z. Cao, B. Ma, C. Wang, Y. Chen, Selective and efficient extraction of lithium from spodumene via nitric acid pressure leaching. *Chem. Eng. Sci.* **287**, 119736 (2024).
17. P. Meshram, B. D. Pandey, T. R. Mankhand, Extraction of lithium from primary and secondary sources by pre-treatment, leaching and separation: A comprehensive review. *Hydrometallurgy* **150**, 192–208 (2014).
18. Q. Yan, X. Li, Z. Wang, X. Wu, H. Guo, Q. Hu, W. Peng, J. Wang, Extraction of valuable metals from lepidolite. *Hydrometallurgy* **117-118**, 116–118 (2012).
19. H. Guo, G. Kuang, H. Wang, H. Yu, X. Zhao, Investigation of enhanced leaching of lithium from α-spodumene using hydrofluoric and sulfuric acid. *Minerals* **7**, 205 (2017).
20. G. Kuang, Y. Liu, H. Li, S. Xing, F. Li, H. Guo, Extraction of lithium from β-spodumene using sodium sulfate solution. *Hydrometallurgy* **177**, 49–56 (2018).
21. F. Lajoie-Leroux, C. Dessemond, G. Soucy, N. Laroche, J. F. Magnan, Impact of the impurities on lithium extraction from β-spodumene in the sulfuric acid process. *Miner. Eng.* **129**, 1–8 (2018).
22. G. D. Rosales, M. del Carmen Ruiz, M. H. Rodriguez, Novel process for the extraction of lithium from β-spodumene by leaching with HF. *Hydrometallurgy* **147-148**, 1–6 (2014).
23. G. D. Rosales, A. C. J. Resentera, J. A. Gonzalez, R. G. Wuilloud, M. H. Rodriguez, Efficient extraction of lithium from β-spodumene by direct roasting with NaF and leaching. *Chem. Eng. Res. Des.* **150**, 320–326 (2019).
24. L. I. Barbosa, J. A. González, M. del Carmen Ruiz, Extraction of lithium from β-spodumene using chlorination roasting with calcium chloride. *Thermochim. Acta* **605**, 63–67 (2015).
25. L. I. Barbosa, G. Valente, R. P. Orosco, J. A. González, Lithium extraction from β-spodumene through chlorination with chlorine gas. *Miner. Eng.* **56**, 29–34 (2014).
26. Y. Chen, Q. Tian, B. Chen, X. Shi, T. Liao, Preparation of lithium carbonate from spodumene by a sodium carbonate autoclave process. *Hydrometallurgy* **109**, 43–46 (2011).
27. L. L. dos Santos, R. Maribondo do Nascimento, S. B. Castellã Pergher, Beta-spodumene: Na_2CO_3:NaCl system calcination: A kinetic study of the conversion to lithium salt. *Chem. Eng. Res. Des.* **147**, 338–345 (2019).
28. G. Zhu, Y. Zhao, X. Zheng, Y. Wang, H. Zheng, D. Lu, Surface features and flotation behaviors of spodumene as influenced by acid and alkali treatments. *Appl. Surf. Sci.* **507**, 145058 (2020).
29. R. Xie, Y. Zhu, J. Liu, Y. Li, The flotation behavior and adsorption mechanism of a new cationic collector on the separation of spodumene from feldspar and quartz. *Sep. Purif. Technol.* **264**, 118445 (2021).
30. R. Xie, Y. Zhu, J. Liu, Y. Li, Flotation behavior and mechanism of α-bromododecanoic acid as collector on the flotation separation of spodumene from feldspar and quartz. *J. Mol. Liq.* **336**, 116303 (2021).
31. H. Zhang, Y. Han, J. Lai, J. Wolf, Z. Lei, Y. Yang, F. Shi, Direct extraction of lithium from ores by electrochemical leaching. *Nat. Commun.* **15**, 5066 (2024).
32. Y. G. Yao, Z. H. Huang, P. F. Xie, S. D. Lacey, R. J. Jacob, H. Xie, F. J. Chen, A. M. Nie, T. C. Pu, M. Rehwoldt, D. W. Yu, M. R. Zachariah, C. Wang, R. S. Yassar, J. Li, L. B. Hu, Carbothermal shock synthesis of high-entropy-alloy nanoparticles. *Science* **359**, 1489–1494 (2018).
33. X. Zheng, X. Gao, R. A. Vila, Y. Jiang, J. Wang, R. Xu, R. Zhang, X. Xiao, P. Zhang, L. C. Greenburg, Y. Yang, H. L. Xin, X. Zheng, Y. Cui, Hydrogen-substituted graphdiyne-assisted ultrafast sparking synthesis of metastable nanomaterials. *Nat. Nanotechnol.* **18**, 153–159 (2023).
34. Y. Chen, G. C. Egan, J. Wan, S. Zhu, R. J. Jacob, W. Zhou, J. Dai, Y. Wang, V. A. Danner, Y. Yao, K. Fu, Y. Wang, W. Bao, T. Li, M. R. Zachariah, L. Hu, Ultra-fast self-assembly and stabilization of reactive nanoparticles in reduced graphene oxide films. *Nat. Commun.* **7**, 12332 (2016).
35. Y. Cheng, J. Chen, B. Deng, W. Chen, K. J. Silva, L. Eddy, G. Wu, Y. Chen, B. Li, C. Kittrell, S. Xu, T. Si, A. A. Martí, B. I. Yakobson, Y. Zhao, J. M. Tour, Flash upcycling of waste glass fibre-reinforced plastics to silicon carbide. *Nat. Sustain.* **7**, 452–462 (2024).
36. K. M. Wyss, J. T. Li, P. A. Advincula, K. V. Bets, W. Chen, L. Eddy, K. J. Silva, J. L. Beckham, J. Chen, W. Meng, B. Deng, S. Nagarajaiah, B. I. Yakobson, J. M. Tour, Upcycling of waste plastic into hybrid carbon nanomaterials. *Adv. Mater.* **35**, e2209621 (2023).
37. Q. Dong, A. D. Lele, X. Zhao, S. Li, S. Cheng, Y. Wang, M. Cui, M. Guo, A. H. Brozena, Y. Lin, T. Li, L. Xu, A. Qi, I. G. Kevrekidis, J. Mei, X. Pan, D. Liu, Y. Ju, L. Hu, Depolymerization of plastics by means of electrified spatiotemporal heating. *Nature* **616**, 488–494 (2023).
38. W. Y. Chen, J. H. Chen, K. V. Bets, R. V. Salvatierra, K. M. Wyss, G. H. Gao, C. H. Choi, B. Deng, X. Wang, T. C. Li, C. Kittrell, N. La, L. Eddy, P. Scotland, Y. Cheng, S. C. Xu, B. W. Li, M. B. Tomson, Y. M. Han, B. I. Yakobson, J. M. Tour, Battery metal recycling by flash Joule heating. *Sci. Adv.* **9**, eadh5131 (2023).
39. B. Deng, X. Wang, D. X. Luong, R. A. Carter, Z. Wang, M. B. Tomson, J. M. Tour, Rare earth elements from waste. *Sci. Adv.* **8**, eabm3132 (2022).
40. A. A. Abdullah, H. C. Oskierski, M. Altarawneh, G. Senanayake, G. Lumpkin, B. Z. Dlugogorski, Phase transformation mechanism of spodumene during its calcination. *Miner. Eng.* **140**, 105883 (2019).
41. A. Buzatu, N. Buzgar, The Raman study of single-chain silicates. *Analele Stiint. ale Univ.* **4**, 107–125 (2010).
42. C. J. S. Pommier, M. B. Denton, R. T. Downs, Raman spectroscopic study of spodumene ($LiAlSi_2O_6$) through the pressure-induced phase change from *C2/c* to $P2_1/c$. *J. Raman Spectrosc.* **34**, 769–775 (2003).
43. U.S. Geological Survey, "Mineral commodity summaries 2024" (U.S. Geological Survey, 2024), 212 pp.; https://doi.org/10.3133/mcs2024 [accessed 30 March 2024].
44. Universal Matter, https://universalmatter.com [accessed 30 March 2024].
45. B. Deng, S. C. Xu, L. Eddy, J. Shin, Y. Cheng, C. Kittrell, K. JeBailey, J. Sharp, L. Qian, S. H. Chen, J. M. Tour, Flash separation of metals by electrothermal chlorination. *Nat. Chem. Eng.* **1**, 627–637 (2024).
46. Gemological Institute of America Inc., Kunzite Description, https://gia.edu/kunzite-description [accessed 30 March 2024].
47. L. Eddy, J. Shin, Y. Cheng, C. H. Choi, C. Teng, P. Scotland, S. C. Xu, A. Lathem, S. H. Chen, Y. M. Han, J. M. Tour, Kilogram flash Joule heating synthesis with an arc welder. *ACS Nano* **18**, 34207–34218 (2024).
48. T. F. O'Brien, T. V. Bommaraju, F. Hine, *Handbook of Chlor-Alkali Technology* (Springer, 2005).
49. K. A. Lokhandwala, S. Segelke, P. Nguyen, R. W. Baker, T. T. Su, I. Pinnau, A membrane process to recover chlorine from chloralkali plant tail gas. *Ind. Eng. Chem. Res.* **38**, 3606–3613 (1999).
50. S. L. Dudarev, G. A. Botton, S. Y. Savrasov, C. J. Humphreys, A. P. Sutton, Electron-energy-loss spectra and the structural stability of nickel oxide: An LSDA+U study. *Phys. Rev. B* **57**, 1505–1509 (1998).
51. K. Reuter, M. Scheffler, Composition, structure, and stability of RuO_2 (110) as a function of oxygen pressure. *Phys. Rev. B* **65**, 035406 (2002).
52. D. R. Stull, H. Prophet, *JANAF Thermochemical Tables, Second Edition* (U.S. National Bureau of Standards, 1971).
53. G. Kresse, J. Furthmuller, Efficient iterative schemes for ab initio total-energy calculations using a plane-wave basis set. *Phys. Rev. B* **54**, 11169–11186 (1996).
54. P. E. Blochl, Projector augmented-wave method. *Phys. Rev. B* **50**, 17953–17979 (1994).
55. J. P. Perdew, K. Burke, M. Ernzerhof, Generalized gradient approximation made simple. *Phys. Rev. Lett.* **77**, 3865–3868 (1996).
56. H. J. Monkhorst, J. D. Pack, Special points for Brillouin-zone integrations. *Phys. Rev. B* **13**, 5188–5192 (1976).
57. O. Peltosaari, P. Tanskanen, E. P. Heikkinen, T. Fabritius, α→γ→β-phase transformation of spodumene with hybrid microwave and conventional furnaces. *Miner. Eng.* **82**, 54–60 (2015).
58. GreenDelta, OpenLCA software, https://openlca.org/ [accessed 1 June 2024].
59. AACE International, "AACE International Recommended Practice No. 56R-08. Cost Estimate Classification System—As Applied in Engineering, Procurement, and Construction for The Building and General Construction Industries" (2020). https://web.aacei.org/docs/default-source/toc/toc_18r-97.pdf [accessed 1 July 2024].

Acknowledgments: The characterization equipment used in this project is partly from the Shared Equipment Authority (SEA) at Rice University. We thank B. Chen of Rice University for helpful input with the XPS results and C. Pennington and T. Terlier for developing ICP-MS methods. **Funding:** The funding of the research was provided by the Defense Advanced

Research Projects Agency (HR00112290122, J.M.T.), the Air Force Office of Scientific Research (FA9550-22-1-0526, J.M.T.), and the US Army Corps of Engineers, ERDC (W912HZ-21-2-0050 and W912HZ-24-2-0027, J.M.T., B.I.Y., and Y.Z.). Computer resources were provided through the DOE NERSC award (BES-ERCAP0027822, B.I.Y.). Y.H. and W.C. acknowledge support from Welch Foundation (C-2065). K.J.S. acknowledges the National Science Foundation Graduate Research Fellowship Program for generous funding. **Author contributions:** Conceptualization: S.X., Q.L., and J.M.T. Construction and maintenance: S.X. and J.Sha. Investigation: S.X., J.Sha., Q.L., L.E., S.C., J.Shi., C.H.C., B.L., and T.S. Characterization: S.X. TEA and LCA: J.Sha. and A.L. GC-MS test: K.J.S. Particle size characterization: W.C. and K.G. DFT computations of the phase structures and thermodynamics trends: Y.Z. and B.I.Y. Writing—draft, review, and editing: S.X., J.Sha., and J.M.T. All aspects of the research were overseen by J.M.T. All authors have discussed the results and given approval to the final version of the manuscript. **Competing interests:** Rice University owns intellectual property on the separation of metals from waste and ores, including spodumene, using FJH with or without concomitant chlorination. Much of this intellectual property has been licensed to a company in which J.M.T. is a shareholder, but he is not an employee, officer, or director in that company. Conflicts of interest are mitigated through disclosure to and compliance with the Rice University Office of Research Integrity. The authors declare that they have no other competing interests. **Data and materials availability:** Source data files (tables S5 to S10) are available at Zenodo: 10.5281/zenodo.15851366. All other data needed to evaluate the conclusions in the paper are present in the paper and/or the Supplementary Materials.

Submitted 29 April 2025
Accepted 3 September 2025
Published 3 October 2025
10.1126/sciadv.ady6457